iScience

CellPress
OPEN ACCESS

Article

Scalable visible light 3D printing and bioprinting using an organic light-emitting diode microdisplay

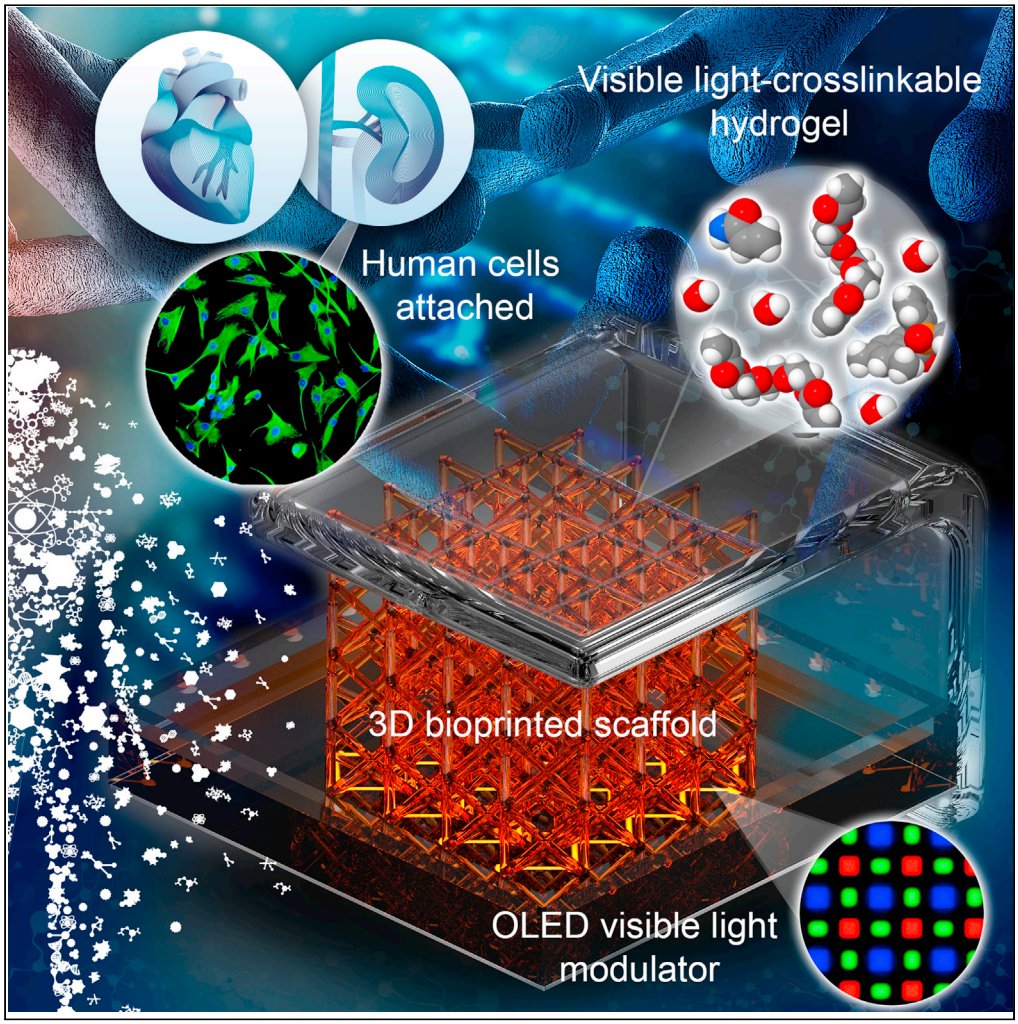

Kavin Kowsari, Wonhye Lee, Seung-Schik Yoo, Nicholas Xuanlai Fang

yoo@bwh.harvard.edu (S.-S.Y.)
nicfang@mit.edu (N.X.F.)

Highlights

We present organic light-emitting diodes (OLED) as a modality of 3D printing

OLED 3D printing offers scalability and high-throughput fabrication at low cost

Averting UV crosslinking, visible light is well-positioned for bioprinted scaffolds

The platform is also capable of multi-material printing

Kowsari et al., iScience 24, 103372
November 19, 2021 © 2021 The Authors.
https://doi.org/10.1016/j.isci.2021.103372

iScience

CellPress
OPEN ACCESS

Article

Scalable visible light 3D printing and bioprinting using an organic light-emitting diode microdisplay

Kavin Kowsari,[1,2] Wonhye Lee,[2] Seung-Schik Yoo,[2,*] and Nicholas Xuanlai Fang[1,3,*]

SUMMARY

To address current unmet needs in terms of scalability and material biocompatibility for future photocrosslinking-based additive manufacturing technologies, emergent platform designs are in inexorable demand. In particular, a shift from the present use of cell-damaging UV light sources in light-based three-dimensional (3D) bioprinting methods demands new platforms. We adopted an organic light-emitting diode (OLED) microdisplay as a digital visible light modulator to create a 3D printing platform modality that offers scalability and multi-material capability while forgoing the need for UV photocrosslinking. We formulate biocompatible inks that are visible light-crosslinkable with relatively quick photoinitiation rates. We demonstrated successful attachment and rapid growth of primary human dermal fibroblast-adult (HDF-a) cells on biological substrates fabricated using the OLED platform. This platform incites new possibilities by providing a simple-yet-effective means for low-cost, high-throughput, and multi-material 3D fabrication of functional structures made of polymers, ceramic composites, and biomaterials.

INTRODUCTION

Industrial part development demands multi-scale production at maximal rates. The multitude of additive manufacturing (AM) methods are increasingly replacing conventional fabrication methods, from nanoscale to mesoscale, owing to the capabilities offered by the many AM modalities to generate unprecedented free-form geometrical complexities by accumulating functional materials in both layered and nonlayered manners (Ngo et al., 2018). Among the various types, the digital light processing (DLP)-based microstereolithography technique exploits localized photopolymerization that selectively converts liquid photopolymer precursors to solidified voxels using high-resolution light projections illuminated at the surface of a photocrosslinkable ink (Sun et al., 2005). Notable advances in DLP-based three-dimensional (3D) fabrication include: (1) submicron printing resolution of multiscale mechanical metamaterials (Zheng et al., 2016), (2) high-throughput volumetric part creation harnessing 3D holographic patterning (Shusteff et al., 2017) or 3D tomographic reconstruction (Kelly et al., 2019), (3) forgoing layer-by-layer printing via continuous liquid interface production (CLIP) (Tumbleston et al., 2015), (4) efficient multi-material microfabrication (Kowsari et al., 2018a; Zhang et al., 2018), (5) grayscale lithography integration to spatially-control crosslink density within structures (Peterson et al., 2016) and to generate micro-lens arrays (Yuan et al., 2019), and rapid high-resolution visible light fabrication (Ahn et al., 2020). Despite the trend of miniaturization in the last decade, recent impactful research is driven by the need for scalability (Saha et al., 2019; Walker et al., 2019; Zheng et al., 2016). Light-based 3D fabrication processes also offer great implications for tissue engineering and bioprinting, from artificial axons to high-resolution 3D hydrogels (Espinosa-Hoyos et al., 2018; Zhang et al., 2018), yet, still met with key challenges. The DLP-based projection microstereolithography (PμSL) technique has been broadly adopted by researchers for its high resolution (e.g., 0.6 μm) and availability in both UV and visible light projection modes (Ahn et al., 2020). It is noteworthy that although the light source of DLP engines are not intrinsically limited to UV light, a large body of DLP platform developments in the literature have employed UV (e.g., 365 nm) or near-UV (405 nm), which increase the likelihood of DNA damage in the case that cells are exposed to the projection during printing (Ge et al., 2020). The chip size of digital micromirror device (DMD) used in the projection imposes limitations on the printable size, hence lateral (*xy* directions, with the *z*-direction representing layer thickness) remain in the millimeter range (Ge et al., 2020), and recent efforts have integrated multiple DLP devices to increase the projection field (Walker et al., 2019).

[1]Department of Mechanical Engineering, Massachusetts Institute of Technology, Cambridge, MA 02139, USA

[2]Department of Radiology, Brigham and Women's Hospital, Harvard Medical School, Boston, MA 02115, USA

[3]Lead contact

*Correspondence: yoo@bwh.harvard.edu (S.-S.Y.), nicfang@mit.edu (N.X.F.)

https://doi.org/10.1016/j.isci.2021.103372

This is an open access article under the CC BY-NC-ND license (http://creativecommons.org/licenses/by-nc-nd/4.0/).

We present our OLED framework as a modality of visible light 3D fabrication, demonstrating the versatile characteristics of the established DLP method, while addressing some of the critical unmet needs. First, OLED microdisplays can cover large areas in microscale to macroscale *via* a single print operation, for example 7-–50-inch OLED displays with micron-sized pixels are available commercially, which are large enough to accommodate human-scale tissue printing. Further panel size enlargement and pixel size reduction are expected in the near-term, evident by recent seminal leaps in OLED technologies that led to achieving 100 times the brightness than those currently commercially available, and smaller pixels smaller than 4 μm, corresponding to high pixel densities, and durability (up to a million hours) (Won et al., 2019). For these reasons, OLED 3D printing is moving toward throughputs demanded by large-scale and industrial-scale additive manufacturing. Second, OLED is the only two-dimensional (2D) digital light modulator with an infinite contrast ratio, a feat that cannot be addressed by commercial DLP light engines and backlit LCD (Liquid Crystal Display) projectors. This is enabled by the emissive nature of organic quantum dot light-emitting diodes that is ideal for cross-linking a layer with zero likelihood of curing residual zones outside the intended digital mask, even after long exposure times. Third, state-of-the-art OLED microdisplays with the highest brightness values and smallest pixels are commercially available at a fraction of the cost of DLP light engines, thereby orienting the OLED platform in the low-cost-yet-effective category. Fourth, the edge-to-edge light intensities of the OLED displays are expected to be uniform, whereas optical elements in DLP projectors can produce darker edges in the field of view relative to the center (Zhou and Chen, 2009). Taken together, these advances render the OLED technology attractive as a 3D printing paradigm. To our knowledge, there are no reports of OLED visible light 3D printing platform, and we herein demonstrate the versatility of this cost-effective AM modality, in light of well-established DLP platforms, paving the course toward photostructured multi-material devices for a plethora of applications that demand advanced polymers, ceramic composites, and biomaterials.

RESULTS AND DISCUSSION

OLED platform and visible light-crosslinkable materials

We transformed a state-of-the-art flexible OLED microdisplay (Samsung Electronics, Figure 1A) into a digital mask modulator for visible light photocrosslinking. The performance comparison plot of Figure 1B shows that even in its first proof-of-concept demo, an off-the-shelf OLED display appears as a promising candidate among other methods that can potentially push the boundaries of 3D printing in terms of scalability. Despite the 15 s/layer OLED curing speed, the solid output speed is lower but close to those of the PμSL/CLIP/volumetric methods. The current system performance does not represent the limit of the OLED process. First, displays equipped exclusively with blue voxels, provided red and green may be omitted as they do not directly contribute to the present method of photoinitiation. This would presumably increase the minimum printable feature size by approximately 2–3 times by eliminating the red/green pixels in the OLED microdisplay. Moreover, recent advances in high-PPI (pixels per inch) μ-OLED displays for near-eye wearables demonstrated pixels less than 4.5 μm in width (Huang et al., 2020; LU et al., 2019).

In the OLED 3D printing process, a 2D layer with a prescribed geometry, corresponding to an OLED-displayed pattern, is crosslinked in a single exposure. Inherently, an entire 2D voxel plate (i.e., layer) is simultaneously crosslinked, attaining much higher throughputs compared to extrusion or droplet platforms' point-to-point, one-dimensional material deposition. As depicted in Figure 1C, the OLED microdisplay was fixed beneath a photopolymer vat (container), the bottom facet of which contained a 50 μm thick, optically clear fluorinated ethylene propylene (FEP) membrane that circumvented adherence of crosslinked layers to the vat. This in turn promoted the bonding of newly solidified layers to the previous solid layer overhead. A motorized *z*-stage elevates the build platform above the microdisplay by a distance equal to the prescribed layer thickness. A pattern pertaining to the sliced first layer is then displayed for the specified exposure duration. The process is repeated for all slices in the series of parallel 2D images through the 3D computer aided design (CAD) file toward formation of a 3D structure (Figure 1D). Automated digital control of the process was orchestrated through a computer program (LabVIEW, National Instruments, Austin, TX, USA). Through refinement of the process parameters (i.e., light intensity, layer thickness, and exposure time), the user can integrate custom-formulated visible light-crosslinkable inks.

Central to the performance of the OLED 3D printing system is formulation of visible light-crosslinkable photopolymers. Photochemical polymerization necessitates light absorption by synthetic/natural chromophores and/or dyes (i.e., photoinitiators) that dissociate to form active species leading to polymerization. Two classes of radical photopolymerization for consideration include Norrish type I initiators that generate

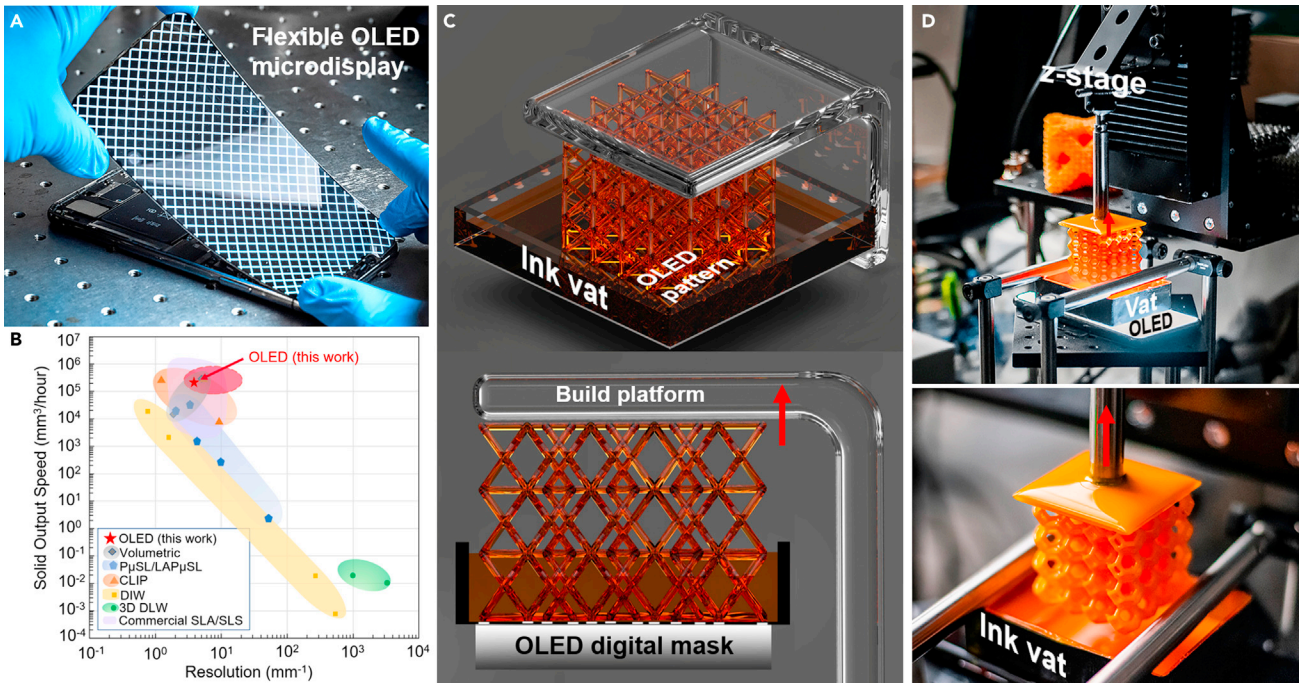

Figure 1. Basic working principles and components of the organic light-emitting diode (OLED) 3D printing system

(A) Flexible OLED microdisplay adopted for use in the present platform.

(B) A process performance comparison of OLED 3D fabrication to other polymer-based 3D printing methods. Resolution is defined as 1/(2δ), where δ is the minimum feature size. Plotted OLED data point is based on the average volume of cured material within three structures, computed using commercial CAD software (SolidWorks, 2021, Dassault Systèmes SolidWorks Corporation, Waltham, MA, USA). Other plotted data points represent published results, commercial manufacturer's specifications, and operating parameters best-known to the authors. Projection microstereolithography (PμSL)/large-area PμSL (LAPμSL), its large-area variant (Zheng et al., 2012, 2014, 2016), continuous liquid interface printing (CLIP) (Tumbleston et al., 2015); direct ink writing (DIW) (Duoss et al., 2007, 2014; Gratson et al., 2006); direct laser writing (DLW); stereolithography (SLA); selective laser sintering (SLS); volumetric (Shusteff et al., 2017). The red dashed boundary represents the authors' speculation regarding the near-term potential of the OLED fabrication method reported in this work.

(C) 3D schematics and (D) photographs of the OLED system components.

initiating radicals via an unimolecular cleavage reaction of an aromatic ketone group, and Norrish type II systems involving benzophenone or quinone derivatives undergoing bimolecular hydrogen abstraction from a co-initiator species to achieve sufficient radical-generation activity (Fouassier et al., 2003). Type I visible light initiators, e.g., (bis(eta 5-2,4-cylcopentadien-1-yl)-bis(2,6-difluoro-3-(1H-pyrrol-1-yl)-phenyl) titanium (Irgacure 784/I784), hexaarylbiimidazoles (HABI), and lithium phenyl-2,4,6-trimethylbenzoylphosphinate (LAP), undergo direct homolysis upon irradiation to yield two active radicals that cleave open vinyl bonds at the acrylate-based functional groups to trigger propagating chain-linking. Such compounds typically exhibit higher radical generation efficiencies than type II systems. Type II photoinitiators for visible light crosslinking have been developed decades for clinical, *in situ* photopolymerization of restorative dental composites. Common type II visible light initiators are camphorquinone (CQ) and Ivocerin in dental resins, as well as Eosin Y, Erythrosine B, fluorescein, rose bengal (RB), riboflavin, and ruthenium-based systems (Fouassier et al., 2010), which are typically used alongside co-initiators to produce sufficient initiating species during conversion of the photoinitiator's carbonyl group into an alcohol. A variety of compounds can be used to facilitate this reaction such as alcohols, ethers, amines, phosphines, and sulfides, however, tertiary aliphatic amines such as ethyl 4-dimethylaminobenzoate (EMDAB) are the most reactive and thereby most frequently used (Andrzejewska et al., 2006).

We adopted Irgacure 784 and CQ-EMDAB as model type I and II initiation systems, respectively, dispersed in 700 Da molecular weight poly (ethylene glycol) diacrylate (PEGDA) along with commercially available resins to create the lattice structures in Figure 2A, with additional structures shown in Figure S1. With a current minimum printable feature size of about 100 μm (Figure 2B), corresponding to a resolution of 5 mm^{-1}, defined as 1/(2δ) (where δ is the minimum feature size) (Shusteff et al., 2017), and a layer thicknesses of

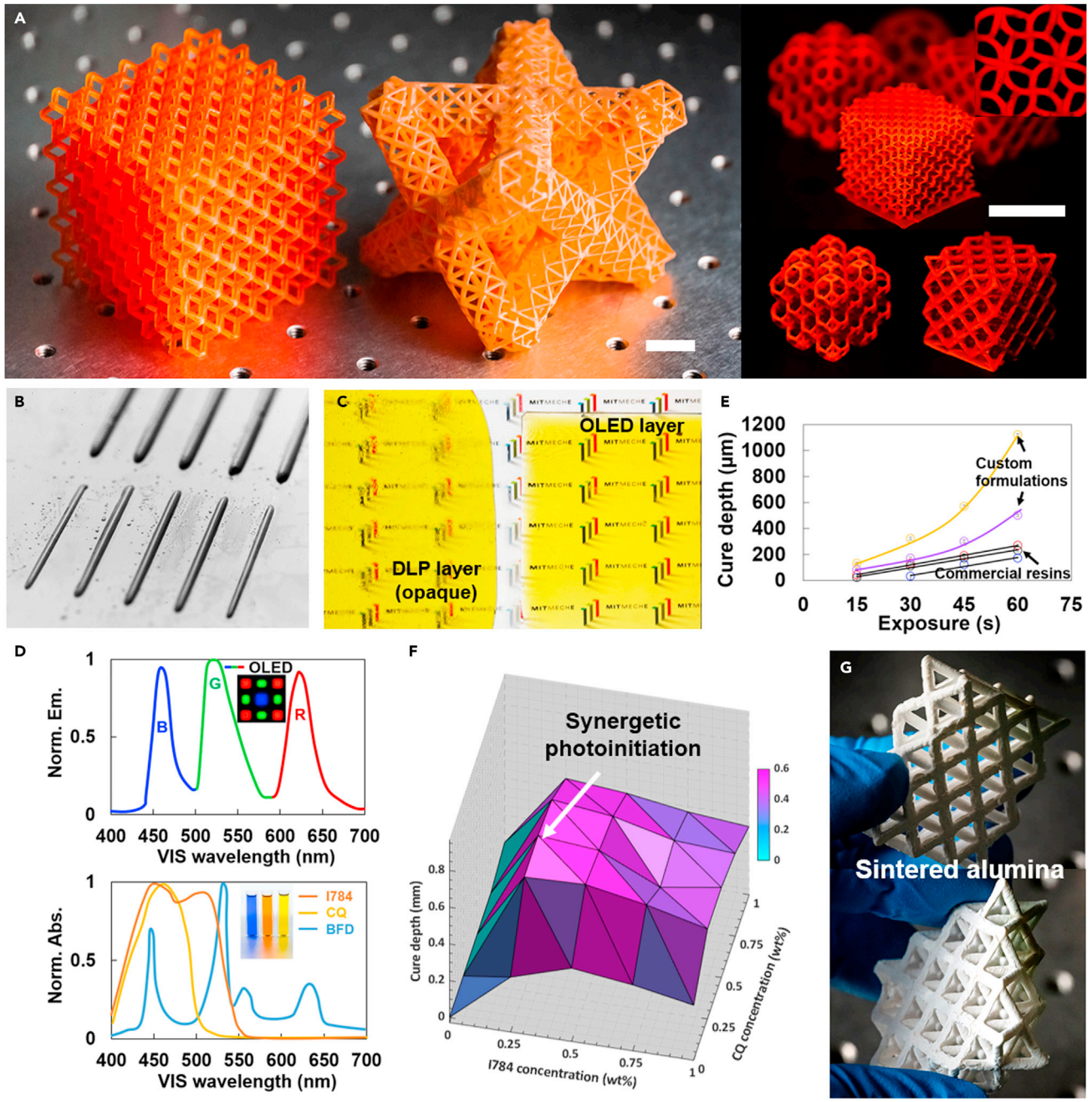

Figure 2. OLED-fabricated structures and self-formulated inks

(A) Structures fabricated using commercial Daylight Hard resin (orange and yellow structures, 250 μm layer thickness, 1 min exposure time), and in-house-formulated ink containing PEGDA 700, 0.5% I784, and 0.001 wt% Rhodamine B (red structures, 50 μm layer thickness, 15 s exposure time). Scale bars represent 16 mm.

(B) Parallel lines 100 μm in width, crosslinked using a 2-pixel wide OLED pattern.

(C) Single-layer opacity comparison between OLED-vs DLP crosslinking methods, using the commercial Daylight resin in both cases. The exposure times for OLED and DLP were 15 s and 1 s, respectively.

(D) Normalized absorption (norm. abs.) of photoinitiators I784, CQ, and blue food dye (BFD), and normalized emission (norm. em.) of the OLED light source.

(E) Jacob's curve comparison between self-formulated (PEGDA-based) vs commercial resins described in the text. Data are represented as mean ± SEM for triplicate measurements for each layer.

Figure 2. *Continued*

(F) 3D plot highlighting the synergetic effect based on the relative concentrations of the constituents of the I784-CQ initiation system. Data are represented as mean values for triplicate measurements for each layer.

(G) Debound structures initially printed with resin containing 700 Da PEGDA, 0.5 wt% I784, and 50 v/w% aluminum oxide nanopowder (50 nm-average diameter) with 100 μm layer thickness, 30 s exposure time. See also Figure S1.

250 μm, parts with overall dimensions up to 70 mm × 70 mm × 70 mm (length × width × height) were fabricated, equivalent to a volumetric throughput of over 300,000 $mm^3 \cdot h^{-1}$, expandable to the current microdisplay size of 160 mm × 70 mm. The optical power of 0.37 $mW \cdot cm^{-2}$, generated by the OLED microdisplay, crosslinked the visible light-sensitive inks at an exposure time of 15 s.

Figure 2C discerns a notable improvement in the optical clarity of individual layers crosslinked with the OLED source vs DLP, signifying the surface smoothness of OLED layers, rendering better overall structure quality. It is hypothesized that this is attributable to the relatively flat light intensity profile across the simulated square pattern shown later in Figure 3B, compared to reported intensity profiles resulting from DLP projections that are known to have wide widths (Emami et al., 2021; Kowsari et al., 2018a; Yuan et al., 2019). Another confounding factor may be the offset between the physical organic light-emitting diodes and the cure plane. Given that each diode emanates light at a wide angle, corresponding to a wide viewing angle, the resulting light intensity distribution at the offset crosslinking plane is smoothed (Figure 3B). Additional ray-tracing models are required to determine the ideal offset yielding the smoothest light intensity profile.

As shown in Figure 2D, I784 absorbs a broader visible spectrum with absorbance peaks of 450 and 510 nm while CQ's sole peak is at 465 nm, whereby in the latter case blue microdiodes were solely contributive to photoinitiation. Importantly, our formulated photopolymers were less viscous and exhibited profoundly faster crosslinking rates of up to 7-fold compared to commercial resins for visible light curing (Daylight Hard, Photocentric, Peterborough, UK) as summarized in Figure 2E. For the present OLED light source, we found EMDAB yielded the highest relative initiation rates as a tertiary amine co-initiator for use alongside CQ (at 1:1 w:w ratio) compared to 4,4′-bis(diethylamino)benzophenone (BDAB) and (2-dimethylaminoethyl) methacrylate (DMAEM).

To further-accelerate photoinitiation, iodonium salt-based synergist, diphenyliodonium hexafluorophosphate (DPIHP), is known to be an efficient initiating electron acceptor that (i) regenerate photoinitiator molecules by replacing inactive, terminating radicals with active, phenyl-initiating radicals, and (ii) generate additional active phenyl radicals (Padon and Scranton, 2000). In three-component systems used in studies involving bulk-curing visible light lamps, photo-differential scanning calorimetry (DSC) has shown parallel reactions occur between the initiator and iodonium and between initiator and amine, yielding increased crosslinking rates compared to two-component systems (Padon and Scranton, 2001). We quantified the synergetic effect of a multi-component photoinitiation ink, containing both types I and II, and observed the highest polymerization rates in hybrid formulations rather than formulations made with individual initiator systems (Figure 2F). Many photoinitiators, including CQ (Asmusen et al., 2009), are known to exhibit photobleaching effects, described as weaker light absorption by photoinitiator products compared to the original photoinitiator molecule, thereby allowing additional light to pass through the system. This effect creates a light intensity gradient in the sample that depends on time and penetration depth into the reaction volume, whereas the initial initiator concentration is uniform. Light penetration can also be precisely controlled by incorporating passive photoabsorbers or opaquing agents into the ink to negate potential unintended crosslinking outside the region of interest, and to limit the layer thickness (Kowsari et al., 2018b). The present OLED platform performed well in fabricating 3D structures without the need for photoabsorbers. It is thought that this presumably arose from the strength of blue light absorption of CQ and I784 photoinitiators used in the inks, or the lower free radical concentrations of the current initiator systems compared to higher-power DLP platforms, as well as the much more localized normal incident light energy dispersion as compared to DLP printing. Augmenting the ink to a multi-component photoinitiator system could be an effective approach to maximize the net crosslinking rate while reducing photobleaching associated with one of the initiating compounds, as evidenced by the relatively smooth increase in layer height as a function of exposure time in Figure 2F.

Nanocomposite lattice structures containing 700 Da PEGDA and 0.5 wt% I784 and 50 v/w% aluminum oxide (alumina) nanopowder (50 nm-average diameter) were photostructured with the OLED platform, with a layer thickness of 100 μm, to produce 'green' parts (a term referred to a part consisting of

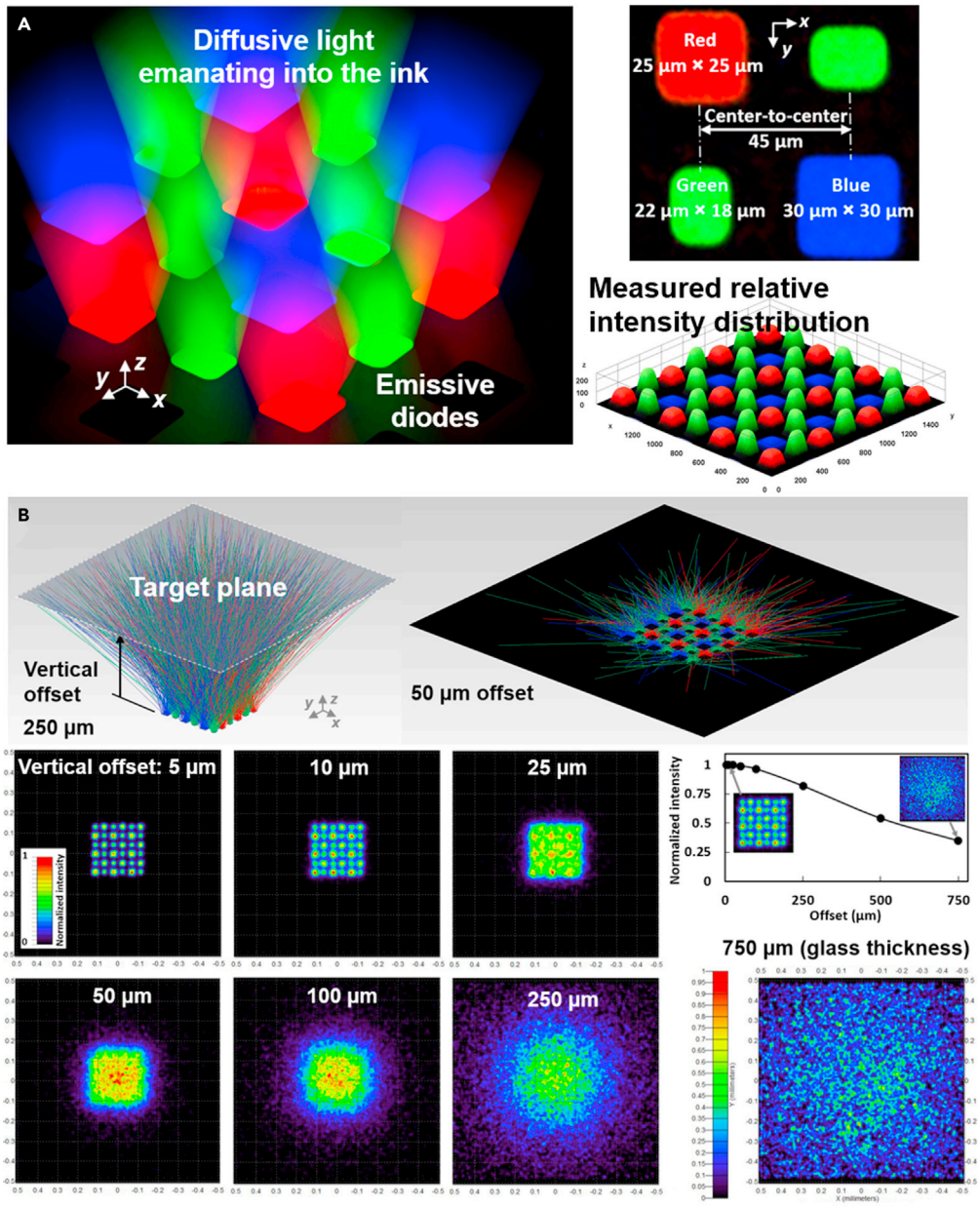

Figure 3. Characterization of the 3D light field generated by the OLED microdisplay

(A) Measured spatial configuration, dimensions, and light intensity distributions.

(B) Ray-tracing simulations of a 6 × 6 emissive OLED array and the corresponding light fields at various offsets away from the surface, i.e., at various cure depths.

particle-embedded polymer composite before pyrolysis). In the present OLED setup, we did not observe any overcuring because of light bleeding outside the photomask, an effect producing crosslinked regions by scattered light as reported in DLP-based fabrication of photopolymers containing >50 vol.% ceramic particles (Huang et al., 2021; Zakeri et al., 2020). The present OLED ceramic printing demonstrates the versatility of the OLED printing platform. Following printing, non-polymerized material was removed by immersion in isopropanol then post-cured for 30 min in a UV-oven (CL-1000, Analytik Jena US). The green part was then thermally debound, i.e., the polymeric matrix was removed by thermal decomposition in a temperature-controlled furnace (FUR-0056, Tabletop Furnace Co.) to a maximum of 1,300°C at a rate of approximately $5°C \cdot m^{-1}$ to create the pyrolyzed ceramic lattice structures in Figure 2G. Similarly, 50 v/w

% silica nanopowder structures were made. Such proof-of-concept results demonstrate the unique capability of the visible light 3D printing platform to allow facile fabrication of highly loaded nano-powder composite inks without sacrificing spatial resolution or other complications during printing. Green parts consisting of ceramic-polymer composites substantially shrink through the pyrolysis process, which we measured to be about 50%, thereby reducing the effective system throughput. Large-area fabrication of OLED 3D printing enables the user to compensate for such large volumetric shrinkages, exceeding the performance of DLP platforms in the context of large-scale photostructured ceramic composite fabrication. These findings warrant future work on achievement of optically transparent glass structures (Kotz et al., 2017) as well as functional ceramics such as niobium pentoxide for photocatalytic applications (Dos Santos et al., 2019) and battery fabrication (Chen et al., 2017).

OLED light field characterization

Measured OLED visible light intensity distribution (Figure 3A) shows a voxel can be approximately modeled as a point spread function, described by a Gaussian distribution as a first-order approximation as (Kang et al., 2012)

$$H\left(x_i, y_j\right) = H_0 e^{-\left(\frac{2}{\omega\left(x_i, y_j\right)^2}\right) r\left(x_i, y_j\right)^2} \quad \text{(Equation 1)}$$

where $H(x_i, y_j)$ is the light intensity distribution and H_0 (mW·cm^{-2}) is the peak intensity at the center of a pixel (x_{i0}, y_{j0}), $r(x_i, y_j)$ is the distance (μm) from the center of the pixel to (x_i, y_j), $\omega(x_i, y_j)$ is the directional Gaussian half-width of the intensity distribution. Here, we adopt a simple exposure threshold model, originally derived as a single-pixel DLP model based on Beer-Lambert law of absorption (Zhao, 2009), then modify the relation to account for differences in the degree of irradiation attenuation through uncrosslinked and crosslinked photopolymer. The expression gives exposure, E, vs depth, z, as

$$E(z) = E_c \frac{\left(D_{pS} e^{\left(\frac{z}{D_{pS}}\right)} + D_{pL} - D_{pS}\right)}{D_{pL}} \quad \text{(Equation 2)}$$

where D_{pL} and D_{pS} are penetration depths (μm) of the liquid photopolymer and a cured, solid layer, respectively, and E_c (mW·cm^{-2}) is the critical energy threshold to trigger photopolymerization, imposed by oxygen inhibition. E_c, D_{pL} and D_{pS}, are obtained by fitting experimental data for a given material system. Integrating a single voxel-based expression (Kang et al., 2012), Equations 1 and 2 are combined to obtain a modified depth-of-cure expression based on the solidified surface position of (x_s, y_s, z_s) (μm, μm, μm) at exposure time, t (s), *as*

$$z_s = -D_{pS} \ln\left[\frac{t}{E_c} \sum_i \sum_j H_0 e^{-\left(2 \times \frac{\sqrt{\left(x_s - \rho\left(i - \left(\frac{m}{2}\right) - 0.5\right)\right)^2 + \left(y_s - \rho\left(j - \left(\frac{n}{2}\right) - 0.5\right)\right)^2}}{\alpha^2 \omega_0^2}\right)} + 2D_{pL}\right] \quad \text{(Equation 3)}$$

where the image size is $m \times n$ pixels, ω_0 (μm) is the Gaussian half-width of the intensity distribution, and α represents the directional variation of the Gaussian half-width, obtained experimentally. It is instructive that, although this simple one-dimensional model provides a direct link between exposure and shape, it overlooks many important intermediate steps such as kinetics of photopolymerization, diffusion effects, and photobleaching, which can strongly influence the predicted overall feature profile (Emami et al., 2021; Miller et al., 2002).

To further-infer the 3D light field generated by the OLED array, we used a ray-tracing simulation software (TracePro, Lambda Research Corp., Littleton, MA, USA) on an equivalent area corresponding to 6 × 6 microdiodes at the OLED surface. Red, green, and blue microdiodes were modeled as emanating surfaces according to the measured wavelength peaks 460, 525, and 625 nm, respectively (Figure 2D). As summarized in Figure 3B, resulting planar fields, simulated at 5, 10, 25, 50, 100, 250, and 750 μm away from the microdiodes, i.e., penetration depths into the liquid photopolymer, the sharpest images delivering the

most precise tolerances occurred at offsets of about 25–50 μm. At an offset equal to the approximate thickness of the manufacturer-bonded glass covering the OLED microdisplay, the simulated image was consequently out-of-focus, necessitating elimination of the protective glass to impart optimal fabrication resolution that increases with proximity to the OLED surface. To this end, we accomplished gentle separation of the glass from the sensitive, flexible OLED microdisplay, and thereby achieved maximum resolution for the commercial display on hand. In addition, glass removal augmented an increase in light intensity of about 65% as in the plot of Figure 3B. In this configuration, two-pixel illuminations produced lines with thicknesses of about 100 μm (Figure 2B), equivalent to a single-pixel size of less than 50 μm. It can also be inferred from the surface plots of Figure 3B that the 50 μm-thick FEP film did not blur the resulting image, hence preserving printing resolution.

Multi-material OLED fabrication

Biomimetic 3D fabrication inspired by natural systems such as wood, nacre, and abalone shells demand hierarchical multi-material structures to harness the synergy between separate domains with disparate properties that can lead to enhancement of mechanical performance (Ge et al., 2020). Additive manufacturing platforms with built-in multi-material capacity offer otherwise unattainable functionalities including, but not limited to, four-dimensional (4D) printing, negative thermal expansion coefficients, and biomimicry. Although multi-material capability is more readily implemented in extrusion methods by simply adding additional extrusion nozzles, it imposes a great challenge for light-based stereolithographic fabrication platforms, necessitating use of multiple vats, cleaning steps, and involving difficulties exchanging liquid photopolymers without cross-contamination (Zhou et al., 2011). Despite this, modified DLP platforms, integrating air jets or dynamic fluidic cell control of multiple liquid photopolymers addressed the difficulties with improved efficiency while minimizing waste (Han et al., 2019; Kowsari et al., 2018a). One such example is our recent work (Kowsari et al., 2018a), which inspired the mechanistic steps for two-material fabrication followed here. First, a 3D CAD model of a structure was sliced into two separate series of bitmap images that correspond to separate inks. The image sets were displayed on the OLED panel in the sequence illustrated in Figure 4A, crosslinking two consecutive layers of one material preceding material exchange, reducing printing time by half. Inks were exchanged by directing an air jet of approximately 1 MPa toward the printed substrate for about 5 s upon removal from the ink, followed by submersion into the alternate ink. The volume of liquid in each vat was maintained at a height of about 1–2 mm over the FEP window to preclude wetting of above layers because of capillary effects, reducing ink cross-contamination. To maintain dimensional accuracy, we forwent the use of solvents such as isopropyl alcohol or ethanol during the material exchange, as cleaning agents are known to warp crosslinked solids and hence loosening part tolerances (Kang et al., 2021). Figure 4B shows demo structures disseminating from the described multi-material protocol, where the materials are distinguished using blue food dye (BFD). As evident in Figure 2D, BFD does not compete with the absorption of the I784 photoinitiator in the 450–525 nm range. Capitalizing on multi-material printing ability, our visible light OLED platform is positioned as a good candidate to create biologically relevant tissue analogues involving multiple compositions of extracellular matrices (ECMs) and different cell types.

Growth of human cells on printed scaffolds

Extracellular biomaterials serve as a structural template to replicate the natural microenvironment, capable of providing signaling factors cells to communicate, migrate, and proliferate. Cells can sense and respond to the surface topography of the ECM by altering their alignment and migration, underlining the importance of bioprinting as an enabling tool for free-form 3D geometrical freedom (Hoffman-Kim et al., 2010). The interplay of the material and processing elements dictates the quality of bioprinted scaffolds for *in vitro* applications such as disease modeling and drug discovery. The two general categories of monomers used to create ECM microenvironments include synthetic vinyl-functionalized (e.g., PEG) and naturally derived hydrogels functionalized with methacrylated groups such as gelatin methacrylate (GelMA) (Miri et al., 2018). Whereas the former provides greater control over molecular weight and distribution and can be better-tailored for mechanical properties, the latter possesses cell attachment motifs that are essential for printed scaffolds.

Here, we report that our visible light 3D fabrication platform and formulated PEG-based hydrogel inks can support attachment and growth of primary human dermal fibroblast-adult (HDF-a) cells. We designed and fabricated grooved 2.5D and 3D bioscaffolds (Figure 5A) with vertical walls forming a 'well' to facilitate the seeding process (not shown in Figures 5A and 5F). Although PEG networks possess intrinsic hydrophilicity and biocompatibility, printed structures had to undergo plasma treatment as a chemical-free means of

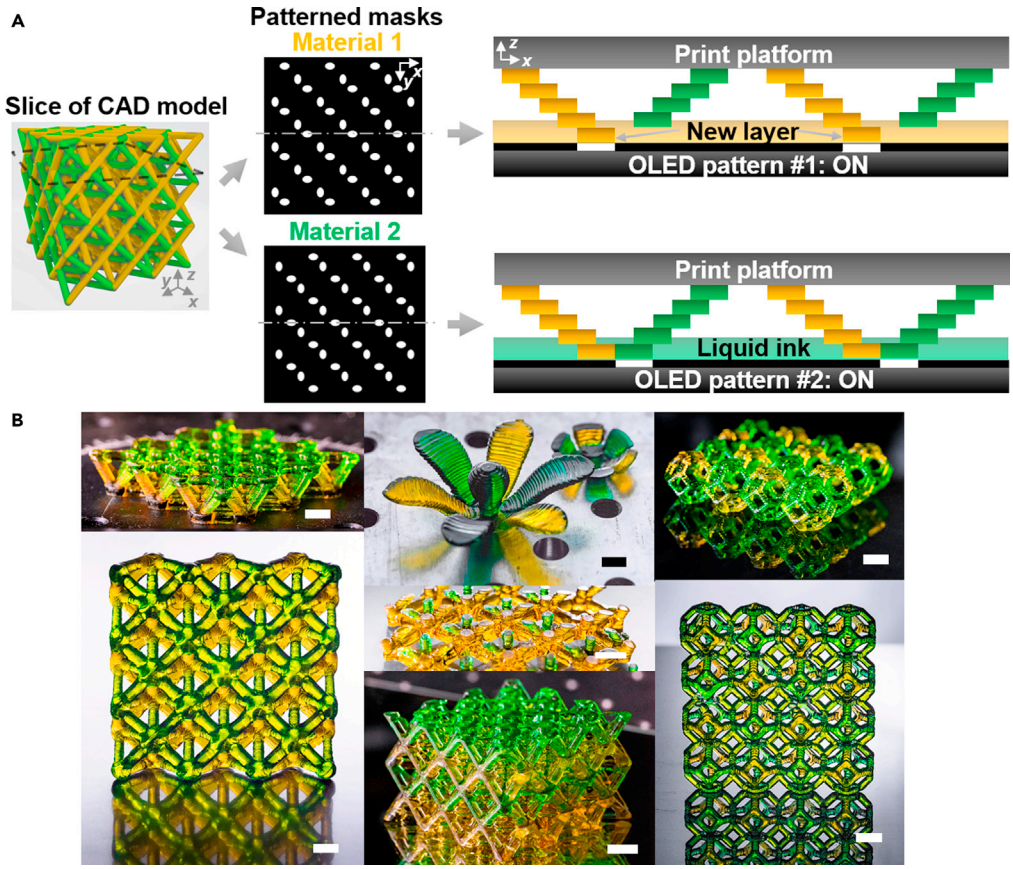

Figure 4. OLED multi-material 3D printing

(A) Schematic of the steps for multi-material fabrication whereby each layer is composed of more than one material.

(B) Sample substrates fabricated using an ink containing PEGDA, 0.5% I784, with and without 0.005% BFD, using the described multi-material protocol with 250 μm layers and 30 s exposures. Scale bars are 5 mm.

introducing biologically relevant functional groups (carbonyl, carboxyl, hydroxyl, and amine) to the PEG backbone. As a result, we observed uniform attachment and rapid differentiation to >95% confluency over a culture period of five days in both 2.5D (Figures 5B–5E) and 3D (Figures 5G–5J) scaffolds. The morphology of fibroblasts attached to the bioprinted scaffolds appeared elongated, suggesting normal proliferation and growth with excellent viability (in green Calcein AM stain) (z-projections in Figures 5D and 5H and volume views in Figures 5E and 5J). Figure 6 shows quantitative cell count and percent cell viability data supporting proliferation of HDF-a cells at passage 8, by about 1.5-fold, and high viability (about 95%) on days 1 and 5, on the PEG-based scaffolds.

Limitations of the study

A number of potential challenges may arise in scaling up the OLED fabrication method to large-scale and industrial-scale applications. First, for meter-scale fabrication, heat generation and buildup from the exothermic photopolymerization reaction becomes a prominent issue. In a recent study, this heat was managed using pumped, non-reactive fluorinated oil bed as buffer between the solidified structure and resin pool to remove interfacial heat (Walker et al., 2019). The OLED device can be retrofitted with an active cooling mechanism to dissipate heat generated in the FEP-ink interface. Second, as part dimensions are expanded, separation of cured layers from the transparent FEP window may become a challenge and necessitate the adoption of ultra-thin polytetrafluoroethylene (PTFE) for enhanced non-stick properties across a wide range of materials. Incorporation of additional modules in the industrialization of our platform is facilitated by the high degree of customizability for its near-term optimization. Third, the high reactivity of visible light-sensitive inks also poses a problem for printing manipulation and storage that may be an issue for practical large-scale applications. We maneuvered this utilizing red light in the otherwise dark

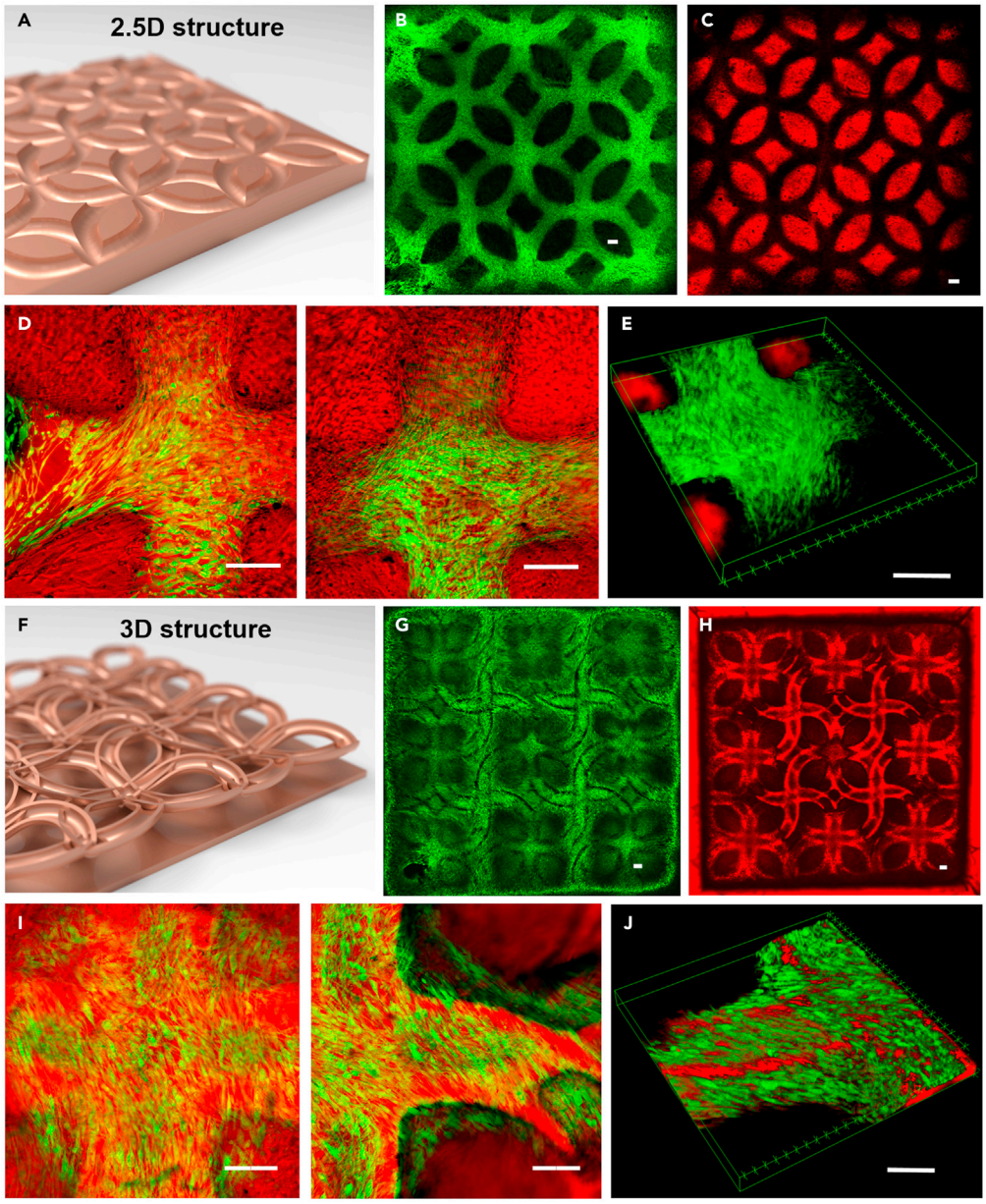

Figure 5. HDF-a attachment and growth on bioprinted structures

(A and F) Designed geometries for 2.5D and 3D microstructures. Vertical walls not shown. 3 × 3 stitched composite images at 4X showing (B and G) calcein AM-stained HDF-a cells in green, as well as (C and H) bioprinted Rhodamine B-tagged (red) scaffolds.

(D and I) Composite 10X z-stacked views demonstrating the elongated morphology of attached fibroblasts.

(E and J) Volumetric views of (D) and (I), respectively. Scale bars are 200 μm.

laboratory space, although the resins did not crosslink under dim daylight for at least several hours. Cautions for proper storage vessels for the photosensitive resins are recommended.

In retrospect, the present findings that primary human cells positively responded to our visible light biological substrate-fabrication process, warrants further research efforts directed toward the practical development of visible light photoinitiators that bypass the potentially detrimental effects of LAP containing toxic lithium, despite its widespread used as a biocompatible photoinitiator (Choi et al., 2019). In addition, testing and utilizing naturally derived hydrogel precursors such as gelatin and hyaluronic acid, along with chemical conjugation

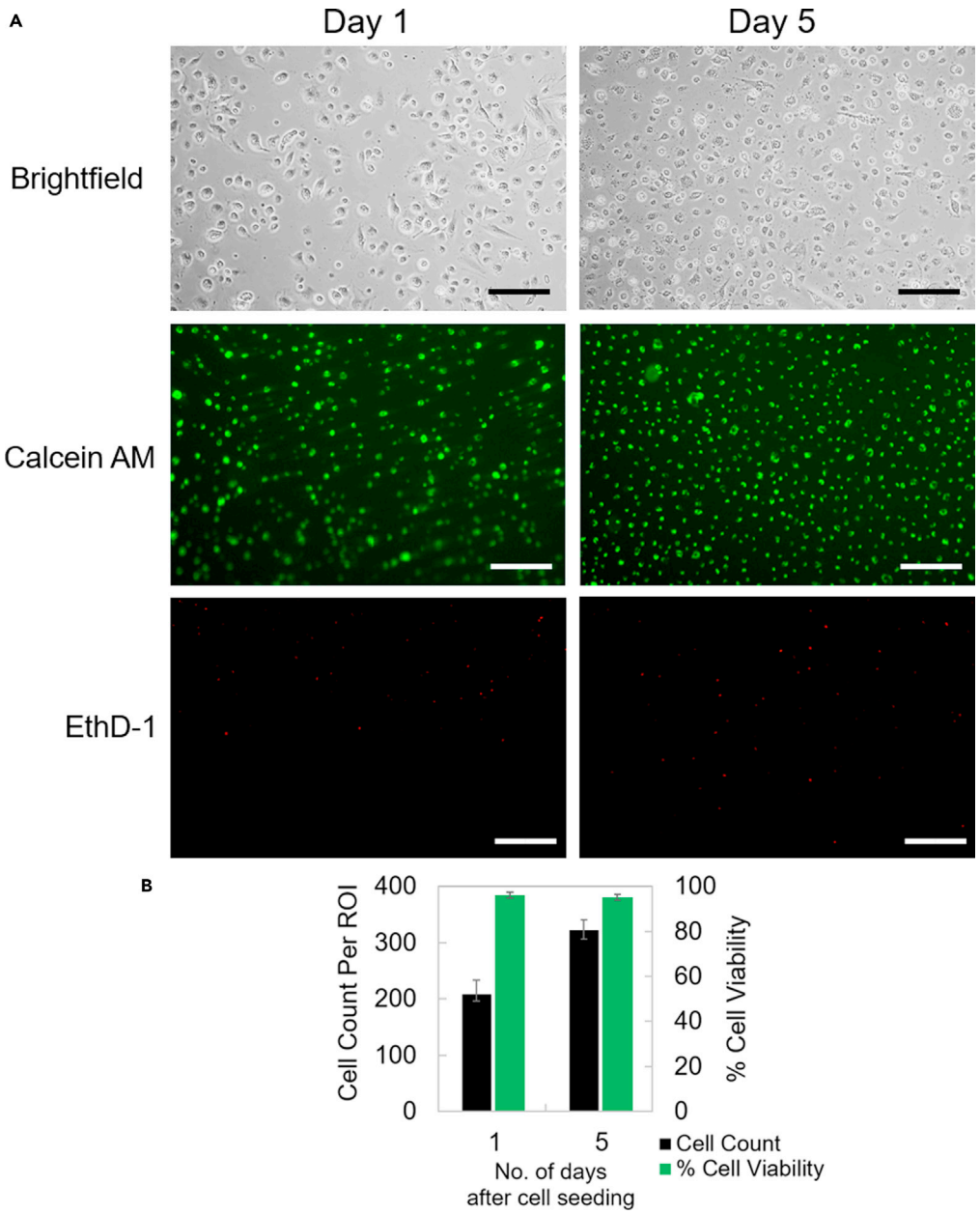

Figure 6. Cell count and viability assay

(A) Representative brightfield (10X) and fluorescent images (4X) for the live (calcein AM, green)-dead (ethidium homodimer-1 (EthD-1), red) viability assay of human fibroblasts at passage 8 on PEGDA scaffold surfaces. Scale bars are 200 μm.

(B) Cell count (number of cells attached to the scaffold surface) and percent cell viability measured on days 1 and 5 after seeding. Each data point represents the mean value of triplicate measurements across three separately created cell-laden scaffolds. Data are represented as mean ± SEM.

(i.e., immobilization) of bioactive cell-attachment motifs such as arginyl-glycyl-aspartic acid (RGD) (Phelps et al., 2012) within synthetic PEG networks remain as the subject of our future work.

Along with the significant recent growth in 3D bioprinting technologies, there are still critical challenges that inhibit the widespread adoption of this emerging technology in the industrial space including the biotechnology sector. In particular, extracellular microenvironment prototyping pursuant to tissue

analogues, possessing improved replication of *in vivo* conditions, demand fabrication processes without the use of cell-damaging UV crosslinking that is currently prominently utilized in current state-of-the-art bioprinting methods. We have addressed some of the unmet needs in a low-cost manner with our OLED platform along with formulations of visible light-crosslinkable, biocompatible materials, inciting new opportunities for high-throughput, multi-material biofidelic tissue engineering.

STAR★METHODS

Detailed methods are provided in the online version of this paper and include the following:

- KEY RESOURCES TABLE
- RESOURCE AVAILABILITY
  - Lead contact
  - Materials availability
  - Data and code availability
- EXPERIMENTAL MODEL AND SUBJECT DETAILS
  - Primary cell cultures
- METHOD DETAILS
  - Platform, materials, and processing
- QUANTIFICATION AND STATISTICAL ANALYSIS

SUPPLEMENTAL INFORMATION

Supplemental information can be found online at https://doi.org/10.1016/j.isci.2021.103372.

ACKNOWLEDGMENTS

K.K. acknowledges the financial support Natural Sciences and Engineering Research Council of Canada (award no. PDF - 529703–2019) and S.-S.Y.'s support using CleCell fund. K.K. thanks Dr. Anna Jagielska and Dr. Daniela Espinosa-Hoyos from Prof. Krystyn van Vliet's Group at MIT for their valuable guidance and allowing us to use their air plasma treatment system. The authors thank Dr. Paula Montero Llopis for her microscopy expertise and support on using Microscopy Resources on the North Quad (MicRoN) core at Harvard Medical School. K.K. also thanks Derek Ouimette for expert technical help on the micro-display's adherent glass separation.

AUTHOR CONTRIBUTIONS

Conceptualization, K.K. and N.X.F.; Methodology, K.K., W.L., S.-S.Y. and N.X.F.; Writing – Original Draft, K.K.; Writing – Review & Editing, K.K., W.L., S.-S.Y. and N.X.F.; Funding Acquisition, K.K., S.-S.Y. and N.X.F.; Supervision, S.-S.Y. and N.X.F.

DECLARATION OF INTERESTS

The authors declare no competing interests.

Received: June 17, 2021
Revised: October 5, 2021
Accepted: October 26, 2021
Published: November 19, 2021

REFERENCES

Ahn, D., Stevens, L.M., Zhou, K., and Page, Z.A. (2020). Rapid high-resolution visible light 3D printing. ACS Cent. Sci. *6*, 1555–1563. https://doi.org/10.1021/acscentsci.0c00929.

Andrzejewska, E., Zych-Tomkowiak, D., Andrzejewski, M., Hug, G.L., and Marciniak, B. (2006). Heteroaromatic thiols as co-initiators for type II photoinitiating systems based on camphorquinone and isopropylthioxanthone. Macromolecules *39*, 3777–3785. https://doi.org/10.1021/ma060240k.

Asmusen, S., Arenas, G., Cook, W.D., and Vallo, C. (2009). Photobleaching of camphorquinone during polymerization of dimethacrylate-based resins. Dent. Mater. *25*, 1603–1611. https://doi.org/10.1016/j.dental.2009.08.010.

Chen, Q., Xu, R., He, Z., Zhao, K., and Pan, L. (2017). Printing 3D gel polymer electrolyte in lithium-ion microbattery using stereolithography. J. Electrochem. Soc. *164*, A1852–A1857. https://doi.org/10.1149/2.0651709jes.

Choi, J.R., Yong, K.W., Choi, J.Y., and Cowie, A.C. (2019). Recent advances in photo-crosslinkable hydrogels for biomedical applications. Biotechniques *66*, 40–53. https://doi.org/10.2144/btn-2018-0083.

Dos Santos, A.J., Batista, L.M.B., Martínez-Huitle, C.A., Alves, A.P.d.M., and Garcia-Segura, S. (2019). Niobium oxide catalysts as emerging material for textile wastewater reuse: Photocatalytic decolorization of azo dyes.

Catalysts *9*, 1070. https://doi.org/10.3390/catal9121070.

Duoss, E.B., Twardowski, M., and Lewis, J.A. (2007). Sol-gel inks for direct-write assembly of functional oxides. Adv. Mater. *19*, 3485–3489. https://doi.org/10.1002/adma.200701372.

Duoss, E.B., Weisgraber, T.H., Hearon, K., Zhu, C., Small, W., IV, Metz, T.R., Vericella, J.J., Barth, H.D., Kuntz, J.D., and Maxwell, R.S. (2014). Three-dimensional printing of elastomeric, cellular architectures with negative stiffness. Adv. Funct. Mater. *24*, 4905–4913. https://doi.org/10.1002/adfm.201400451.

Emami, M.M., Jamshidian, M., and Rosen, D. (2021). Multiphysics modeling and experiments of grayscale photopolymerization with application to microlens fabrication. J. Manuf. Sci. Eng. *143*, 091005. https://doi.org/10.1115/1.4050549.

Espinosa-Hoyos, D., Jagielska, A., Homan, K.A., Du, H., Busbee, T., Anderson, D.G., Fang, N.X., Lewis, J.A., and Van Vliet, K.J. (2018). Engineered 3D-printed artificial axons. Sci. Rep. *8*, 478. https://doi.org/10.1038/s41598-017-18744-6.

Fouassier, J.-P., Morlet-Savary, F., Lalevée, J., Allonas, X., and Ley, C. (2010). Dyes as photoinitiators or photosensitizers of polymerization reactions. Materials *3*, 5130–5142.

Fouassier, J., Allonas, X., and Burget, D. (2003). Photopolymerization reactions under visible lights: Principle, mechanisms and examples of applications. Prog. Org. Coat. *47*, 16–36. https://doi.org/10.1016/S0300-9440(03)00011-0.

Ge, Q., Li, Z., Wang, Z., Kowsari, K., Zhang, W., He, X., Zhou, J., and Fang, N.X. (2020). Projection micro stereolithography based 3D printing and its applications. Int. J. Extreme Manuf. *2*, 022004. https://doi.org/10.1088/2631-7990/ab8d9a.

Gratson, G.M., García-Santamaría, F., Lousse, V., Xu, M., Fan, S., Lewis, J.A., and Braun, P.V. (2006). Direct-write assembly of three-dimensional photonic crystals: Conversion of polymer scaffolds to silicon hollow-woodpile structures. Adv. Mater. *18*, 461–465.

Han, D., Yang, C., Fang, N.X., and Lee, H. (2019). Rapid multi-material 3D printing with projection micro-stereolithography using dynamic fluidic control. Addit. Manuf. *27*, 606–615.

Hoffman-Kim, D., Mitchel, J.A., and Bellamkonda, R.V. (2010). Topography, cell response, and nerve regeneration. Annu. Rev. Biomed. Eng. *12*, 203–231. https://doi.org/10.1146/annurev-bioeng-070909-105351.

Huang, X., Dai, H., Hu, Y., Zhuang, P., Shi, Z., and Ma, Y. (2021). Development of a high solid loading β-TCP suspension with a low refractive index contrast for DLP-based ceramic stereolithography. J. Eur. Ceram. Soc. *41*, 3743–3754. https://doi.org/10.1016/j.jeurceramsoc.2020.12.047.

Huang, Y., Hsiang, E.-L., Deng, M.-Y., and Wu, S.-T. (2020). Mini-LED, micro-LED and OLED displays: Present status and future perspectives. Light: Sci. Appl. *9*, 1–16. https://doi.org/10.1038/s41377-020-0341-9.

Kang, H.-W., Park, J.H., and Cho, D.-W. (2012). A pixel based solidification model for projection based stereolithography technology. Sens. Actuators A *178*, 223–229. https://doi.org/10.1016/j.sna.2012.01.016.

Kang, S., Chang, S.-Y., Costa, A., Kowsari, K., and Ma, A.W. (2021). Additive manufacturing of embedded carbon nanocomposite structures with multi-material digital light processing (MMDLP). J. Mater. Res. 1–10. https://doi.org/10.1557/s43578-021-00224-3.

Kelly, B.E., Bhattacharya, I., Heidari, H., Shusteff, M., Spadaccini, C.M., and Taylor, H.K. (2019). Volumetric additive manufacturing via tomographic reconstruction. Science, eaau7114. https://doi.org/10.1126/science.aau7114.

Kotz, F., Arnold, K., Bauer, W., Schild, D., Keller, N., Sachsenheimer, K., Nargang, T.M., Richter, C., Helmer, D., and Rapp, B.E. (2017). Three-dimensional printing of transparent fused silica glass. Nature *544*, 337. https://doi.org/10.1038/nature22061.

Kowsari, K., Akbari, S., Wang, D., Fang, N.X., and Ge, Q. (2018a). High-efficiency high-resolution multimaterial fabrication for digital light processing-based three-dimensional printing. 3D Print. Addit. Manuf. *5*, 185–193. https://doi.org/10.1089/3dp.2018.0004.

Kowsari, K., Zhang, B., Panjwani, S., Chen, Z., Hingorani, H., Akbari, S., Fang, N.X., and Ge, Q. (2018b). Photopolymer formulation to minimize feature size, surface roughness, and stair-stepping in digital light processing-based three-dimensional printing. Addit. Manuf. *24*, 627–638. https://doi.org/10.1016/j.addma.2018.10.037.

LU, P., Huang, G., Yang, S., Chen, X., Dong, X., Wang, H., Wang, Y., Xuan, M., Zhang, C., and Yang, M. (2019). 52-4: Highest PPI Micro-OLED Display Sustain for Near-eye Application (Wiley Online Library), pp. 725–726.

Miller, G., Gou, L., Narayanan, V., and Scranton, A. (2002). Modeling of photobleaching for the photoinitiation of thick polymerization systems. J. Polym. Sci. A: Polym. Chem. *40*, 793–808.

Miri, A.K., Nieto, D., Iglesias, L., Goodarzi Hosseinabadi, H., Maharjan, S., Ruiz-Esparza, G.U., Khoshakhlagh, P., Manbachi, A., Dokmeci, M.R., and Chen, S. (2018). Microfluidics-enabled multimaterial maskless stereolithographic bioprinting. Adv. Mater. *30*, 1800242. https://doi.org/10.1002/adma.201800242.

Ngo, T.D., Kashani, A., Imbalzano, G., Nguyen, K.T., and Hui, D. (2018). Additive manufacturing (3D printing): A review of materials, methods, applications and challenges. Compos. B Eng. *143*, 172–196. https://doi.org/10.1016/j.compositesb.2018.02.012.

Padon, K.S., and Scranton, A.B. (2000). A mechanistic investigation of a three-component radical photoinitiator system comprising methylene blue, N-methyldiethanolamine, and diphenyliodonium chloride. J. Polym. Sci. A Polym. Chem. *38*, 2057–2066. https://doi.org/10.1002/(SICI)1099-0518(20000601)38:11<2057::AID-POLA140>3.0.CO;2-5.

Padon, K.S., and Scranton, A.B. (2001). A mechanistic investigation of the three-component radical photoinitiator system eosin Y spirit soluble, N-methyldiethanolamine, and diphenyliodonium chloride. J. Polym. Sci. A Polym. Chem. *39*, 715–723. https://doi.org/10.1002/1099-0518(20010301)39:5<715::AID-POLA1043>3.0.CO;2-O.

Peterson, G.I., Schwartz, J.J., Zhang, D., Weiss, B.M., Ganter, M.A., Storti, D.W., and Boydston, A.J. (2016). Production of materials with spatially-controlled cross-link density via vat photopolymerization. ACS Appl. Mater. Interfaces *8*, 29037–29043. https://doi.org/10.1021/acsami.6b09768.

Phelps, E.A., Enemchukwu, N.O., Fiore, V.F., Sy, J.C., Murthy, N., Sulchek, T.A., Barker, T.H., and García, A.J. (2012). Maleimide cross-linked bioactive peg hydrogel exhibits improved reaction kinetics and cross-linking for cell encapsulation and in situ delivery. Adv. Mater. *24*, 64–70. https://doi.org/10.1002/adma.201103574.

Saha, S.K., Wang, D., Nguyen, V.H., Chang, Y., Oakdale, J.S., and Chen, S.-C. (2019). Scalable submicrometer additive manufacturing. Science *366*, 105–109. https://doi.org/10.1126/science.aax8760.

Schindelin, J., Arganda-Carreras, I., Frise, E., Kaynig, V., Longair, M., Pietzsch, T., Preibisch, S., Rueden, C., Saalfeld, S., and Schmid, B. (2012). Fiji: An open-source platform for biological-image analysis. Nat. Methods *9*, 676–682.

Schneider, C.A., Rasband, W.S., and Eliceiri, K.W. (2012). NIH Image to ImageJ: 25 years of image analysis. Nat Methods *9*, 671–675.

Shusteff, M., Browar, A.E., Kelly, B.E., Henriksson, J., Weisgraber, T.H., Panas, R.M., Fang, N.X., and Spadaccini, C.M. (2017). One-step volumetric additive manufacturing of complex polymer structures. Sci. Adv. *3*, eaao5496. https://doi.org/10.1126/sciadv.aao5496.

Sun, C., Fang, N., Wu, D., and Zhang, X. (2005). Projection micro-stereolithography using digital micro-mirror dynamic mask. Sens. Actuators, A *121*, 113–120. https://doi.org/10.1016/j.sna.2004.12.011.

Tumbleston, J.R., Shirvanyants, D., Ermoshkin, N., Janusziewicz, R., Johnson, A.R., Kelly, D., Chen, K., Pinschmidt, R., Rolland, J.P., and Ermoshkin, A. (2015). Continuous liquid interface production of 3D objects. Science *347*, 1349–1352. https://doi.org/10.1126/science.aaa2397.

Walker, D.A., Hedrick, J.L., and Mirkin, C.A. (2019). Rapid, large-volume, thermally controlled 3D printing using a mobile liquid interface. Science *366*, 360–364. https://doi.org/10.1126/science.aax1562.

Won, Y.-H., Cho, O., Kim, T., Chung, D.-Y., Kim, T., Chung, H., Jang, H., Lee, J., Kim, D., and Jang, E. (2019). Highly efficient and stable InP/ZnSe/ZnS quantum dot light-emitting diodes. Nature *575*, 634–638. https://doi.org/10.1038/s41586-019-1771-5.

Yuan, C., Kowsari, K., Panjwani, S., Chen, Z., Wang, D., Zhang, B., Ng, C.J.-X., Alvarado, P.V.y., and Ge, Q. (2019). Ultrafast three-dimensional printing of optically smooth microlens arrays by oscillation assisted digital light processing. ACS

Appl. Mater. Interfaces. https://doi.org/10.1021/acsami.9b14692.

Zakeri, S., Vippola, M., and Levänen, E. (2020). A comprehensive review of the photopolymerization of ceramic resins used in stereolithography. Addit. Manuf. *35*, 101177. https://doi.org/10.1016/j.addma.2020.101177.

Zhang, B., Li, S., Hingorani, H., Serjouei, A., Larush, L., Pawar, A., Goh, W., Sakhaei, A., Hashimoto, M., Kowsari, K., et al. (2018). Highly stretchable hydrogels for UV curing based high-resolution multimaterial 3D printing. J. Mater. Chem. B *6*, 3246–3253. https://doi.org/10.1039/C8TB00673C.

Zhao, X. (2009). Process Planning for Thick-Film Mask Projection Micro Stereolithography (Georgia Institute of Technology).

Zheng, X., Deotte, J., Alonso, M.P., Farquar, G.R., Weisgraber, T.H., Gemberling, S., Lee, H., Fang, N., and Spadaccini, C.M. (2012). Design and optimization of a light-emitting diode projection micro-stereolithography three-dimensional manufacturing system. Rev. Sci. Instrum. *83*, 125001. https://doi.org/10.1063/1.4769050.

Zheng, X., Lee, H., Weisgraber, T.H., Shusteff, M., DeOtte, J., Duoss, E.B., Kuntz, J.D., Biener, M.M., Ge, Q., and Jackson, J.A. (2014). Ultralight, ultrastiff mechanical metamaterials. Science *344*, 1373–1377. https://doi.org/10.1126/science.1252291.

Zheng, X., Smith, W., Jackson, J., Moran, B., Cui, H., Chen, D., Ye, J., Fang, N., Rodriguez, N., and Weisgraber, T. (2016). Multiscale metallic metamaterials. Nat. Mater. *15*, 1100–1106. https://doi.org/10.1038/nmat4694.

Zhou, C., and Chen, Y. (2009). Calibrating Large-Area Mask Projection Stereolithography for its Accuracy and Resolution Improvements. Proceedings of Solid Freeform Fabrication 2009, Austin, TX, USA. http://edge.rit.edu/content/P10551/public/SFF/SFF%202009%20Proceedings/2009%20SFF%20Papers/2009-09-Zhou.pdf.

Zhou, C., Chen, Y., Yang, Z., and Khoshnevis, B. (2011). Development of Multi-Material Mask-Image-Projection-Based Stereolithography for the Fabrication of Digital Materials. Proceedings of Solid Freeform Fabrication 2011, Austin, TX, USA. http://utw10945.utweb.utexas.edu/Manuscripts/2011/2011-06-Zhou.pdf.

STAR★METHODS

KEY RESOURCES TABLE

REAGENT or RESOURCE	SOURCE	IDENTIFIER
Chemicals, peptides, and recombinant proteins		
Poly(ethylene glycol) diacrylate (PEGDA) monomer	Sigma-Aldrich, St. Louis, MO, USA	Cat#455008
Aluminum oxide nanopowder	Sigma-Aldrich, St. Louis, MO, USA	544833
Silica nanopowder	Sigma-Aldrich, St. Louis, MO, USA	718483
4,4′-Bis(diethylamino)-benzophenone (BDAB) co-initiator	Sigma-Aldrich, St. Louis, MO, USA	160326
Ethyl 4-dimethylaminobenzoate (EDMAB) co-initiator	Sigma-Aldrich, St. Louis, MO, USA	8.41086
(2-dimethylaminoethyl) methacrylate (DMAEM) co-initiator	Sigma-Aldrich, St. Louis, MO, USA	234907
Diphenyliodonium hexafluorophosphate (DPIHP) iodonium salt synergist	Sigma-Aldrich, St. Louis, MO, USA	548014
Rhodamine B (fluorescent dye)	Sigma-Aldrich, St. Louis, MO, USA	83689
(Bis(eta 5-2,4-cylcopentadien-1-yl)-bis(2,6-difluoro-3-(1H-pyrrol-1-yl)- phenyl) titanium (Irgacure 784/I784) photoinitiator	IGM Resins USA Inc., Charlotte, NC, USA	N/A
Lithium phenyl-2,4,6-trimethylbenzoylphosphinate (LAP) photoinitiator	Sigma-Aldrich, St. Louis, MO, USA	900889
Daylight hard (3D printing resin)	Photocentric, Peterborough, UK	DAYHDGY01
Critical commercial assays		
LIVE/DEAD Viability/Cytotoxicity Kit	Invitrogen, Waltham, MA, USA	Cat#L3224
Deposited data		
Visible light absorption spectra data for photoinitiators and emission spectra for OLED	This paper; Mendeley Data	https://doi.org/10.17632/r8nzht4kjg.1
Experimental models: Cell lines		
Primary adult human dermal fibroblasts (HDF-a)	ScienCell Research Laboratories, Inc., Carlsbad, CA, USA	Cat#2320
Fibroblast medium (FM)	ScienCell Research Laboratories, Inc., Carlsbad, CA, USA	Cat#2301
Fetal bovine serum (FBS)	ScienCell Research Laboratories, Inc., Carlsbad, CA, USA	Cat#0010
Fibroblast growth serum (FGS)	ScienCell Research Laboratories, Inc., Carlsbad, CA, USA	Cat#2352
Penicillin/streptomycin (P/S solution)	ScienCell Research Laboratories, Inc., Carlsbad, CA, USA	Cat#0503
TrypLE Express reagent	Invitrogen, Waltham, MA, USA	Cat#12605010
Software and algorithms		
ImageJ	Schneider et al., 2012	https://imagej.nih.gov/ij/
Image display and motorized stage control code	This paper; Mendeley Data, using NI LabVIEW 2020 (National Instruments Corporation (NI), Austin, TX, USA)	https://doi.org/10.17632/mrwxxy5576.1
Ray-tracing simulation software	This paper; Mendeley Data, using TracePro, Lambda Research Corp., Littleton, MA, USA	https://doi.org/10.17632/99yz9ndym5.1
Other		
Performance comparison plot data of Figure 1B	Shusteff et al., 2017	https://doi.org/10.1126/sciadv.aao5496

RESOURCE AVAILABILITY

Lead contact

Further information and requests for resources and reagents should be directed to and will be fulfilled by the Lead Contact, Nicholas X. Fang (nicfang@mit.edu).

Materials availability

This study did not generate new unique reagents.

Data and code availability

- *Data* Spectroscopy and raytracing simulation data have been deposited at Mendeley Data and are publicly available as of the date of publication. DOIs are listed in the key resources table. All data reported in this paper will be shared by the lead contact upon request.
- *Code* All original code has been deposited at Mendeley Data and is publicly available as of the date of publication. DOIs are listed in the key resources table.
- Any additional information required to reanalyze the data reported in this paper is available from the lead contact upon request.

EXPERIMENTAL MODEL AND SUBJECT DETAILS

Primary cell cultures

Primary adult human dermal fibroblasts (HDF-a, 2320, ScienCell Research Laboratories, Inc., Carlsbad, CA, USA) were grown to 90-95% confluency in 75-cm^2 tissue culture flasks (TPP Techno Plastic Products AG, Trasadingen, Switzerland) at 37°C under 5% CO_2 atmosphere using complete medium containing fibroblast medium (FM, 2301, ScienCell Research Laboratories, Inc., Carlsbad, CA, USA), 2% fetal bovine serum (FBS, 0010, ScienCell Research Laboratories, Inc.), 1% fibroblast growth serum (FGS, 2352, ScienCell Research Laboratories, Inc.), and 1% penicillin/streptomycin (P/S solution, 0503, ScienCell Research Laboratories, Inc.). Cells were grown in T75 tissue culture flasks (TPP Techno Plastic Products AG, Trasadingen, Switzerland) with routine culture media exchange every 3 days as per the vendor's protocols and dissociated (TrypLE Express reagent, Invitrogen, Waltham, MA, USA). HDF-a cells were seeded at passage 10 were as a suspension with a cell density of $\sim 10^6$ cells/mL in culture media and a seeding volume of 0.25 mL, seeded on bioprinted structures, which were then placed in 12-well tissue culture plates and maintained similarly as those in T75 flasks. For the fluorescence and confocal microscopy images, cells were stained with 2 μM calcein AM and 4 μM ethidium homodimer-1 (EthD-1) working solutions in Dulbecco's phosphate-buffered saline (DPBS, Invitrogen, Waltham, MA, USA) for 45 min at 37°C under 5% CO_2 atmosphere, according to the live/dead viability kit (LIVE/DEAD Viability/Cytotoxicity Kit, Invitrogen, Waltham, MA, USA).

METHOD DETAILS

Platform, materials, and processing

The mechanical components of the platform were sourced from Thorlabs, Inc. Newton, NJ, USA, consisting of base plates, posts and post assemblies, and a *z*-stage (NRT100, Thorlabs Inc., Newton, NJ, USA), with a bidirectional repeatability of 1 μm. The 3 mm-thick borosilicate glass used as the build platform was obtained from McMaster-Carr Supply Company, Elmhurst, IL, USA. The FEP film was sourced from Photocentric, Peterborough, UK, and secured over the OLED microdisplay using vat tape from the same supplier.

Monomer, poly(ethylene glycol) diacrylate (PEGDA), aluminum oxide (alumina) nanopowder and silica nanopowder, photoinitiator components, 4,4′-bis(diethylamino)benzophenone (BDAB), ethyl 4-dimethylaminobenzoate (EDMAB), (2-dimethylaminoethyl) methacrylate (DMAEM), diphenyliodonium hexafluorophosphate (DPIHP), and lithium phenyl-2,4,6-trimethylbenzoylphosphinate (LAP), as well as fluorescent dye, Rhodamine B, were obtained from Sigma-Aldrich, St. Louis, MO, USA and used without further purification. Photoinitiator (bis(eta 5-2,4-cylcopentadien-1-yl)-bis(2,6-difluoro-3-(1H-pyrrol-1-yl)- phenyl) titanium (Irgacure 784/I784) was purchased from IGM Resins USA Inc., Charlotte, NC, USA. For the bioprinted scaffolds, 80 wt% PEGDA (700 Da) in deionized water was used a solvent of 0.15 wt% LAP photoinitiator and 0.001 wt% Rhodamine B. The structures were fabricated using a custom-built visible light projector system (exposure time of 30 s and layer thickness of 50 μm), then treated to air plasma (ATTO B, Diener electronic

GmbH, Ebhausen, Germany) for 5 min. Printed samples were kept in distilled water and removed immediately prior to placement in the plasma treatment chamber. The samples were resubmerged in DPBS and used in the seeding experiments within two hours of plasma treatment, following exposure to the UV light of a biosafety cabinet for 30 min.

QUANTIFICATION AND STATISTICAL ANALYSIS

Acellular/cellular substrates were imaged using brightfield and fluorescent microscopes (EVOS FL Auto 2, Invitrogen, Waltham, MA, USA; and Inverted Phase Contrast Microscope, Nikon Corp., Tokyo, Japan). Cell count (number of cells) and percent viability for the number of cells attached to the scaffold surface) were performed in three different regions of interest (ROI), spanning a 1.2 mm by 0.8 mm field of view (FOV), in three separate flat layers (triplicates), whereby statistical details of the measurements can be found in the caption of Figure 6. A sample size of ~9 was computed to be large enough to distinguish biological variability from natural variance using a typical power calculation value (1-β) of 0.9 at α=0.01, with corresponding Type I/Type II error = 0.01/0.1. A paired t-test ($p<0.05$) was performed on the acquired values to compare the cell viability on days 1 and 5 after seeding.

Layer thicknesses were quantified with a 20X objective lens attached to CMOS sensor (Nikon Corp., Tokyo, Japan) using three separately crosslinked layers for each data point, whereby statistical details of the measurements can be found in the caption of Figure 2. UV-VIS spectrometer (USB2000+VIS-NIR-ES, Ocean Optics Inc., Orlando, FL, USA) was used for absorption measurements of the photopolymer constituents including the photoinitiators as well as the emissive spectra of the OLED microdisplay. A 200 μL puddle containing 0.25 wt% of the ink was placed on a glass coverslip, placed over the brightfield microscope, whereby the illumination passed through the liquid and was captured with the spectrometer photodiode above. The spectra of the solvents (i.e., PEGDA in the cases of P784 or CQ and distilled water in the case of blue food dye), were subtracted. The OLED light intensity was measured using a photodiode power sensor attached to a power meter console covering the 400-700 nm-wavelength visible range (PM100D and S120VC, Thorlabs, Newton, NJ, USA). A white image was displayed at full intensity and the photodiode was held facing the OLED microdisplay while a measurement was recorded.

Fluorescence confocal microscopy (IX83, Olympus Corp., Tokyo, Japan) was performed using two fluorescent channels (calcein AM and Rhodamine B), and *z*-stacked cross-sectional images were acquired with a distance of 2 μm between each step. ImageJ (Schindelin et al., 2012) software was used to stack the images. Cell seeding density was measured using a hemocytometer containing 9 square counting grids (Neubauer Improved (NI) grid), each 1 mm^2 in a chamber having a volume of 10 μL (C-Chip, INCYTO, Chungnam-do, South Korea). Cells were manually counted in the four corner grids and the average number of cells was multiplied by 10,000 to determine the cell density in units of cells/mL, according to the vendor's protocols.